Fracture penetration and proppant transport in gas- and foam-fracturing

Jiehao Wang [*], Derek Elsworth [**]

Department of Energy and Mineral Engineering, EMS Energy Institute and G3 Center, Pennsylvania State University, University Park, PA, 16802, USA

A B S T R A C T

Gases show promise as an alternative to water-based fracturing fluids because they are non-damaging to water-sensitive formations, show some potential to create complex fracture networks, flow back to the well rapidly after treatment, and deliver some environmental benefits. However, the ability of gases to transport proppant has been questioned due to their relatively low viscosity and density. The fracturing then proppant-carrying capacity of various gases is investigated to determine the form and function of the emplaced proppant pack. First, fracture propagation and proppant transport driven by several commonly-used pure gases (CO_2, liquified petroleum gas, ethane, and N_2) is simulated and compared against slickwater fracturing – generally identifying inferior reach and functionality. Several methods are then investigated to improve the proppant-carrying capacity of the pure gases. Results show that, compared with slickwater, gases create shorter and narrower fractures and carry proppant shorter distances due to their lower viscosity and faster leak-off. Among the gases examined in this study, liquified petroleum gas and CO_2 return the deepest proppant penetration along the fracture, followed by ethane, and with N_2 unable to carry proppant into the fracture due to the resulting narrow fracture. However, elevating injection rate of gases could improve their fracture-inducing potential and proppant-transport capability to a level competitive with that of slickwater. A near-uniform proppant distribution may be achieved by using a gelled gas, with an approximately two order-of-magnitude enhancement in viscosity, or a foam-based fluid with a high quality. The fracture length may also be extended by limiting leak-off due to the increased viscosity. Moreover, ultra-light-weight proppants (ULWPs) perform better with gases than commonly-used sands in terms of uniformity of distribution, due to decelerated proppant settling. Well performance is improved significantly by fracturing with gelled gases or foams instead of pure gases or by pumping ULWPs instead of normal sands.

1. Introduction

Hydraulic fracturing is one of the most effective and widely-used methods to stimulate production from unconventional oil and gas reservoirs exhibiting micro- and nano-Darcy native permeability. This requires the pumping of highly-pressurized fracturing fluids into wells to create new fractures or reactivate pre-existing natural fractures in the hydrocarbon-bearing reservoir. A proppant pad is introduced later in the pumping and fracture-driving sequence to prop open the complex network of fractures when pumping ultimately stops and fractures deflate under the *in situ* stress. These fracture networks provide direct contact between the wellbore and the reservoir and drastically increase the contact area with highly conductive channels enabling the hydrocarbon to be effectively recovered.

Slickwater, composed of water and a small amount of friction reducer, is currently the most popular fracturing fluid used in commercial production of unconventional oil and gas. This is due to its low cost, ready availability, as well as its ability to generate complex fracture networks with good fracture containment and limited gel damage within fractures (Palisch et al., 2010). However, its dependence on significant volumes of water has led to a series of issues. First, water-induced formation damage might impair productivity in water-sensitive reservoirs due to significant capillary effects and potentially high contents of swelling clay (Xu et al., 2016). Second, slickwater fracturing entails massive amount of water, which places significant stress on local water resources, especially for the areas suffering from water deficits (Gallegos et al., 2015). Additionally, disposal of large volumes of flow back fluids by deep reinjection is recognized as a significant cause for the increasing number of induced low-level earthquakes observed over the last decade (Ellsworth, 2013; Elsworth et al., 2016). All of these concerns promote

Table 1
Comparisons among three commonly-used gaseous fracturing fluids (CO_2, N_2, and LPG).

Gases	Advantages	Disadvantages
CO_2	Good miscibility with hydrocarbons improving oil mobility and recovery; Accelerated desorption of adsorbed gas in formations; Potential sequestration of greenhouse gases underground.	Corrosive nature of CO_2 in presence of water; Limited availability in some locations; Requirement of gas separation before hydrocarbon production; Possible leak of CO_2 to the atmosphere.
N_2	Good availability and low cost of gaseous N_2; Inert gas having no chemical interactions with rock formations; Potential to create self-propped fractures by thermal shock.	Low density preventing N_2 from being applied in deep reservoirs; Special equipment required to handle low-temperature liquid N_2.
LPG	Full compatibility with reservoirs since LPG and hydrocarbons are mutually soluble; Reduced flaring; Possibility of 100% recovery of the LPG in the well production stream.	High safety risk due to the explosive nature of LPG; High investment cost.

the research and development of alternative stimulation methods, including the use of waterless fracturing agents.

A few waterless fracturing technologies have been developed and field tested during the past several decades, including oil-based fracturing, explosive and propellant fracturing, and gas fracturing (Wang et al., 2016). Among them, gas fracturing has recently attracted considerable research effort (Middleton et al., 2015; Gan et al., 2015; Li et al., 2016; Bennour et al., 2017; Wang et al., 2020). This is because gas fracturing can not only avoid the problems encountered by water-based fracturing methods but also delivers other benefits. Gas fracturing allows the fracture to be created and the proppant to be placed by gases in their liquid or supercritical phases. At reservoir equilibrium pressure and temperature, the gases will transit to their vapor phase, which completely eliminates any capillary-pressure damage as well as results in a rapid flowback after treatment (Lillies and King, 1982). Moreover, gases are recognized to have the potential to generate complex fracture networks in formations (Ishida et al., 2016; Wang et al., 2018c). These complex fracture networks provide a large contact area between the wellbore and the reservoir, which favors a high production rate. In addition, greenhouse gases may be sequestered underground as they are working as fracturing fluids (Middleton et al., 2015). Various pure gases have been used as fracturing fluids in field demonstrations where CO_2, N_2, and liquified petroleum gas (LPG) are the most common. Detailed reviews of the various fracturing techniques with these gases are available and documented (Gandossi, 2013; Moridis, 2018) with comparisons among them summarized in Table 1. However, the low viscosities and densities of gases, relative to those of room-temperature liquids, may result in limited proppant-carrying capacity and reduced fracture-inducing potential (narrow apertures), both of which could be obstacles preventing gas fracturing from being widely applied. Nonetheless, although the effectiveness of gases as fracturing fluids has been questioned, relevant studies are surprisingly limited, and the effect of low fluid viscosity on fracture propagation and proppant placement is poorly understood.

Various methods can be used to enhance the proppant-carrying capacity of gases. In some cases, a gas is gelled before fracturing to achieve a high and consistent viscosity, which is able to evenly distribute the proppant in fractures (King, 1983; Tudor et al., 2009). Most recently, foam-based fluids have been found useful in well stimulation (Wanniarachchi et al., 2015, 2017). Generally, foams can be made by mixing a gas with a liquid, where gas bubbles are encased in a liquid phase cage. The two-phase fluid flow nature of foams provides a high viscosity mixture with low liquid content - ensuring improved proppant-carrying capacity and a favorable suitability for water-sensitive reservoirs. In addition, the development of ultra-light-weight proppants (ULWPs) also shows promise for gas fracturing. ULWPs are usually 25%–60% lighter than commonly-used sands, but sufficiently strong to withstand reservoir stresses (Gu et al., 2015). Due to the low density, the settling velocity of ULWPs is much lower than that of the commonly-used sands, enabling them to be carried further downrange along fluid-driven fractures.

Precise prediction of fracture geometries remains a significant challenge due to the extraordinary complexity of active processes. Most "traditional" hydraulic fracturing models have been developed based on the linear elastic fracture mechanics with simple 2D or pseudo-3D geometry (Khristianovic and Zheltov, 1955; Perkins and Kern, 1961; Greetesma and de Klerk, 1969; Nordgren, 1972; Adachi et al., 2007; Dontsov and Peirce, 2015a; Wang et al., 2018a). By making reasonable simplifications, these models provide both fast and efficient solution to define fracture evolution and extent – and their routine utilization in the oil and gas industry. Recent desires are to improve the fidelity of predictions with more realistic descriptions of key influencing factors - accommodating true 3D fracture geometry, interaction between the hydraulic fracture and geological discontinuities, and creation of complex fracture networks. To achieve this, a variety of numerical methods have been utilized, such as finite element methods (FEM) with cohesive zone elements (Chen et al., 2009; Carrier and Granet, 2012) or continuum damage mechanics approaches (Wang et al., 2018c; Liu et al., 2018a), extended finite element methods (XFEM) (Gordeliy and Peirce, 2013), discrete element methods (Zhang et al., 2017a, Zhang et al., 2019a), distinct element methods (Damjanac and Cundall, 2016; Ghaderi et al., 2018), and boundary element methods (Zhang et al., 2007). Comprehensive reviews of the literature are available for both traditional (Detournay, 2016; Lecampion et al., 2018) and advanced (Taleghani et al., 2016) hydraulic fracturing models. Proppant transport poses an additional challenge to the modelling of hydraulic fracturing. The transport of solid particles (proppant) is often approached as a volumetric concentration of proppant by using Eulerian-Eulerian models (Ouyang et al., 1997; Shiozawa and McClure, 2016) or Eulerian-Lagrangian models (Dontsov and Peirce, 2015b; Zhang et al., 2017b). These continuum methods are widely used due to their simplicity and high efficiency, although some aspects of the physics (such as collisions and friction between particles) are ignored. CFD-DEM (Computational Fluid Dynamics-Discrete Element Method) models offer the potential to incorporate the true physics but with high computational cost and often relegated to solve only subsets of the full problem (Zeng et al., 2016). Reviews of models representing proppant transport are also available (Osiptsov, 2017).

In this study, we investigate the ability of different gases to transport proppant in a propagating blade-shaped fracture and then evaluate the resulting gas production rates using previously developed deformation-transport-closure models (Wang et al., 2018a, 2018b; Wang and Elsworth, 2018). The numerical models are first briefly introduced, followed by numerical simulations of fracture propagation and proppant transport driven by slickwater, CO_2, N_2, ethane, and LPG. Following this, we examine the proppant-carrying capacity of gelled gases and foam-based fluids as well as the performance of ULWPs carried by gases. Finally, fracture conductivities of all the cases are calculated and input into reservoir simulations to evaluate gas production rates.

2. Deformation-transport-closure models

We explore fracture propagation coupled with proppant transport using an internally consistent model satisfying the elastic stress

distribution with transport of a rheological mixture of fracturing fluid and proppant (Wang et al., 2018a, 2018b). A fracture closure model is then used to follow the evolution of the residual aperture profile and conductivity of fractures partially filled with proppant packs as the hydraulic pressure decreases at the conclusion of pumping (Wang and Elsworth, 2018).

2.1. Fracture propagation

Fracture propagation is formulated based on the PKN-formalism (Perkins and Kern, 1961; Nordgren, 1972), representing a simplified model with a pre-constrained fracture geometry. The model assumes propagation of a vertical blade-shaped fracture of constant height and elliptical cross-section, as illustrated in Fig. 1. The constant-height assumption limits the model to the condition where the contrast in horizontal stress between pay zone and bounding zones is sufficiently high. Plane strain is enforced in the plane perpendicular to the direction of propagation, fluid pressure in the fracture is assumed uniform with height and the toughness of the rock is assumed negligible. These conditions are likely reasonable for large blade-like fractures. However, most importantly for this work, the PKN model is a useful test bed for modelling proppant transport and fracture deflation in this work – as it provides a consistent platform to evaluate differences in the performance with different fracturing fluids – where all other characteristics are held constant. It should be also noted that this study is mainly focused on proppant transport driven by gases in the main hydraulic fractures without considering any secondary fractures or fracture networks. Thus, a planar fracturing model (PKN) is sufficient to capture this behavior. However, for the situation where large and extensive distributions of natural fractures exist, more advanced fracturing models are required to accommodate the resulting fracture network and the complex proppant distribution (Park et al., 2001; Taleghani et al., 2016; Liu et al., 2018b; Zhang et al., 2019a, 2019b).

The fracture width profile is given by

$$w(x,z,t) = \frac{2(1-\nu^2)}{E}\left(H^2 - 4z^2\right)^{1/2} p(x,t), \tag{1}$$

where $0 \leq x \leq l(t)$, $-\frac{H}{2} \leq z \leq \frac{H}{2}$, and t are the horizontal and vertical coordinates and time, respectively. Herein, $l(t)$ represents fracture length; H is the fracture height; E is the Young's modulus; ν is the Poisson's ratio and $p(x,t) = p_f(x,t) - \sigma_h$ is the net fluid pressure inside the fracture with $p_f(x,t)$ the absolute fluid pressure and σ_h the *in situ* stress acting perpendicular to the plane of the fracture.

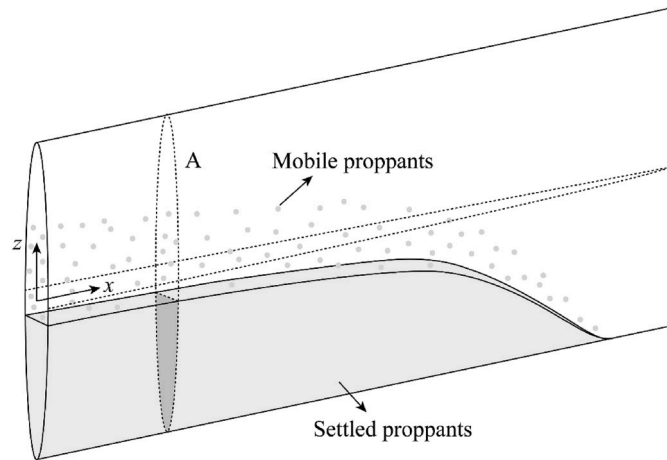The flux of the fluid/slurry within the fracture can be defined by

Fig. 1. Schematic of proppant transport in a propagating blade-shaped fracture. The fracture is assumed to have a constant height and an elliptical cross-section (see the cross-section A for an illustration).

Poiseuille's law as

$$q^s(x,z,t) = -\frac{w^3(x,z,t)}{12\mu_f}\widehat{Q}^s\left[\overline{\varphi}(x,z,t), \frac{w(x,z,t)}{a}\right]\frac{\partial p(x,t)}{\partial x}, \tag{2}$$

where μ_f is the dynamic viscosity of the clear fracturing fluid; a is the proppant particle radius; $\widehat{Q}^s$ is a dimensionless function of $\overline{\varphi} = \varphi/\varphi_{max}$ and w/a with φ the volumetric concentration of proppant and φ_{max} the maximum allowable volumetric concentration determined from geometrical considerations. The function $\widehat{Q}^s$ is introduced by Dontsov and Peirce (2014) based on an empirical constitutive model which is able to capture the transition from Poiseuille flow to Darcy filtration flow as the normalized proppant concentration $\overline{\varphi}$ increases from 0 to 1, as illustrated by Fig. 2a.

By considering fracture inflation, fluid flow and fluid leak-off, the local fluid mass balance equation is written as

$$\frac{\partial \overline{w}(x,t)}{\partial t} + \frac{\partial \overline{q}^s(x,t)}{\partial x} + \frac{2C_l}{\sqrt{t - \tau(x)}} = 0. \tag{3}$$

where $\overline{w}(x,t) = \frac{1}{H}\int_{-H/2}^{H/2} w(x,z,t)\mathrm{d}z$ and $\overline{q}^s(x,t) = \frac{1}{H}\int_{-H/2}^{H/2} q^s(x,z,t)\mathrm{d}z$ are the average width and flux over the fracture height, respectively, the constant C_l is the Carter leak-off coefficient, and $\tau(x)$ is the time at which the fracture leading edge arrives at location x. The gaseous fracturing fluids are treated as incompressible in this study due to their high pressure and near-liquid state when retained in liquid or supercritical phases – fluid pressure and density only change slightly during the fracturing. Therefore, it is reasonable to model this problem using the averaged density and viscosity of the fracturing fluids.

The fracture propagation model is defined by Eqs. (1)–(3), which is complemented by the initial conditions given by a small time asymptotic solution (Kovalyshen and Detournay, 2010) and the boundary conditions at the inlet and the fracture tip as

$$\overline{q}^s(0,t) = Q_0 / 2H \quad \text{and} \quad \overline{w}(l,t) = 0 \tag{4}$$

where Q_0 is the injection rate for a bi-wing fracture. Together with the proppant concentration field $\overline{\varphi}(x,z,t)$ obtained by the proppant transport model to be introduced below, this set of equations is sufficient to determine the evolution of the fracture footprint defined by $l(t)$ and H, and the field quantities $w(x,z,t)$, $q^s(x,z,t)$ and $p(x,t)$.

2.2. Proppant transport

The 2D mass balance equation for the proppant is written as

$$\frac{\partial w(x,z,t)\overline{\varphi}(x,z,t)}{\partial t} + \frac{\partial q_x^p(x,z,t)}{\partial x} + \frac{\partial q_z^p(x,z,t)}{\partial z} = 0. \tag{5}$$

where q_x^p and q_z^p respectively represent the proppant flux in the x and z directions. The fluxes can be defined as

$$q_x^p = B\left(\frac{w}{a}\right)\widehat{Q}^p\left(\overline{\varphi}, \frac{w}{a}\right)q^s, \tag{6}$$

$$q_z^p = -B\left(\frac{w}{a}\right)\frac{a^2 w}{12\mu_f}(\rho_p - \rho_f)g\widehat{G}^p\left(\overline{\varphi}, \frac{w}{a}\right), \tag{7}$$

where ρ_p and ρ_f are densities of the proppant particle and clear fracturing fluid, respectively, and g is the gravitational acceleration. $\widehat{Q}^p$ and $\widehat{G}^p$ are two dimensionless functions of the proppant concentration $\overline{\varphi}$ and the ratio w/a (Dontsov and Peirce, 2014) and describe pressure-driven proppant convection and proppant settling, respectively, as illustrated in Fig. 2b and (c). B is a blocking function, accounting for proppant bridging which occurs when the fracture width is only of the order of several diameters of the proppant particles [see Fig. 2d].

Validations of fracture propagation and proppant transport are
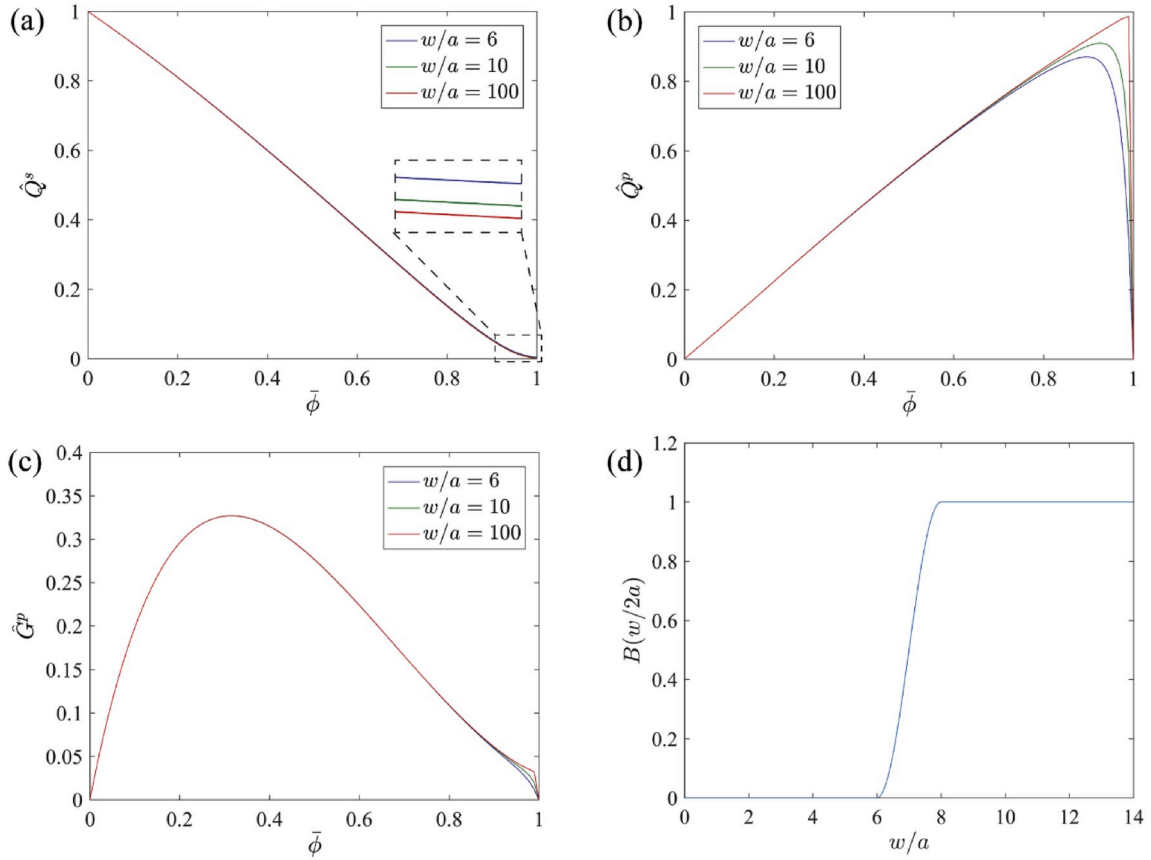
Fig. 2. The functions (a) $\widehat{Q}^s$, (b) $\widehat{Q}^p$ and (c) $\widehat{G}^p$ introduced by Dontsov and Peirce (2014) versus normalized proppant concentration for 3 specified values of the parameter w/a, and (d) the blocking function $B(w/a)$ versus the parameter $w/2a$, assuming proppant bridging occurs when the fracture width is 3 times the diameter of the proppant particles.

described separately (Wang et al., 2018a, 2018b) together with detailed description of the numerical algorithm solving these two equation systems (Wang et al., 2018a).

2.3. Residual aperture and conductivity of closed fractures

During shut-in, flowback and production stages, decreasing hydraulic pressure allows the fracture to deflate and to compact the encased proppant pack. A fracture closure model is then used to follow the evolution of the residual aperture profile and conductivity of fractures partially filled with proppant packs as the hydraulic pressure decreases at the conclusion of pumping (Wang and Elsworth, 2018). The fracture closure model introduced here is capable of accommodating the mechanical response of the proppant pack, fracture closure of potentially contacting rough surfaces, proppant embedment into fracture walls, and most importantly flexural displacement of the unsupported spans of the fracture.

Based on linear elasticity, the residual width profile $w_r(x,z)$ and the net stress applied on the fracture walls $\sigma_n(x,z)$ can be related by an integral equation as

$$w_r(x,z) = \frac{4}{\pi E'} \int_{-H/2}^{H/2} \sigma_n(x,s) G(z,s) ds - 2w_e(x,z), \tag{8}$$

where $w_e(x,z)$ is the depth of proppant embedment multiplied by a factor 2 accounting for the embedment into both walls of the fracture, and $G(z,s)$ is a singular elastic kernel expressed as (Tada et al., 2000)

$$G(z,s) = \cosh^{-1} \frac{H^2 - 4sz}{2H|z-s|}. \tag{9}$$

Note that the integral in Eq. (8) has to be understood in the sense of a Cauchy principal value.

The net stress applied on the fracture walls $\sigma_n(z)$ can be viewed as a superposition of far-field stress acting perpendicular to the plane of the fracture σ_h, fluid pressure within the fracture $p_f(x,z)$, back stress from the proppant pack $\sigma_p(x,z)$, and back stress from the fracture asperities $\sigma_a(x,z)$:

$$\sigma_n(x,z) = p_f(x,z) + \sigma_p(x,z) + \sigma_a(x,z) - \sigma_h. \tag{10}$$

Assuming that the proppant pack has a constant compressibility c_p, the stress field driving compaction can be written as

$$\sigma_p(x,z) = \begin{cases} \dfrac{1}{c_p} \ln \dfrac{w_{r0}(x,z)\overline{\varphi}_{r0}(x,z)}{w_r(x,z)}, & w_r(x,z) < w_{r0}(x,z)\overline{\varphi}_{r0}(x,z) \\ 0, & w_r(x,z) \geq w_{r0}(x,z)\overline{\varphi}_{r0}(x,z) \end{cases}, \tag{11}$$

where w_{r0} and $\overline{\varphi}_{r0}$ are the fracture width and proppant concentration when pumping stops. They both have a subscript 0 because the conditions at the end of the pumping defines the initial conditions for the fracture closure analysis. The product of w_{r0} and $\overline{\varphi}_{r0}$ gives the initial width of the proppant pack.

For the unpropped fracture regions, roughness of fracture walls controls the closure of the two elastic surfaces in contact. The contact stress of the asperity can be described as (Bandis et al., 1983; Barton et al., 1985)

$$\sigma_a(x,z) = \begin{cases} \dfrac{w_a - w_r(x,z)}{b_1 - b_2[w_a - w_r(x,z)]}, & w_r(x,z) < w_a \\ 0, & w_r(x,z) \geq w_a \end{cases} \tag{12}$$

where w_a is the asperity width, b_1 is a constant representing the compliance of the asperity, and $b_2 = b_1/w_a$. Note that this model gives $\sigma_a(x,z) = 0$ at $w(x,z) \geq w_a$ and an infinite $\sigma_a(x,z)$ as $w(x,z)$ goes to zero, implying that the fracture is not allowed to completely close.

Based on elastic Hertzian contact theory, the depth of proppant embedment can be written as

$$w_e(x,z) = \begin{cases} a\left(\dfrac{3\pi}{4E'}\right)^2 \left[\dfrac{16\eta E'^2}{9\pi^3 c_p} \ln \dfrac{w_{r0}(x,z)\overline{\varphi}_{r0}(x,z)}{w_r(x,z)}\right]^{2/3}, & w_r(x,z) < w_{r0}(x,z)\overline{\varphi}_{r0}(x,z), \\ 0, & w_r(x,z) \geq w_{r0}(x,z)\overline{\varphi}_{r0}(x,z) \end{cases}$$
(13)

where $\eta \geq 2\sqrt{3}$ is a constant determined by the proppant packing.

Given the fluid pressure distribution within the fracture $p_f(x,z)$, the residual profile of the fracture aperture $w_r(x,z)$ can be obtained by the integral equation, *i.e.* Eq. (13), combined with Eqs. (14)–(18). Following this, the conductivity of the compacted proppant packs and the unpropped fracture regions can be obtained by the cubic law and the Kozeny-Carman model, respectively, as

$$C(x,z) = \begin{cases} \dfrac{w_r^3(x,z)}{12}\widehat{Q}^s\left[\overline{\varphi}_r(x,z), \dfrac{w_r(x,z)}{a}\right], & w_r(x,z) \geq w_{r0}(x,z)\overline{\varphi}_{r0}(x,z) \\ w_r(x,z)\dfrac{a^2}{45}\dfrac{n_r^3(x,z)}{[1 - n_r(x,z)]^2}, & w_r(x,z) < w_{r0}(x,z)\overline{\varphi}_{r0}(x,z) \end{cases}$$
(14)

where $\overline{\varphi}_r(x,z) = w_{r0}(x,z)\overline{\varphi}_{r0}(x,z)/w_r(x,z)$ is the residual proppant concentration, and $n_r(x,z) = 1 - \overline{\varphi}_r(x,z)\varphi_{max}$ is the residual porosity of the proppant pack.

Eqs. (8)–(13) are first solved for the residual aperture of the closed fracture, w_r, by using a displacement discontinuity method (Wang and Elsworth, 2018). Fracture conductivity, C, can then be evaluated by Eq. (14).

Sections 2.1-2.3 define the deformation-transport-closure models which are employed to investigate gas fracturing, proppant transport, and the resulting production rate in this study. These models have been benchmarked against analytical solutions and existing numerical solutions (Wang et al., 2018a, 2018b; Wang and Elsworth, 2018).

3. Results and discussions

We perform a series of numerical simulations on fracture propagation and proppant transport driven by various gases, including CO_2, N_2, Ethane, and LPG, and compare these against standard slickwater fracturing. Since fracture lengths and proppant reach for fracturing with gases is generally less effective than with slickwater, we investigate the performance of gelled gases and foam-based fluids and ultra-lightweight proppants (ULWPs) transported by gases.

3.1. Gas fracturing and proppant transport

Consider a formation at a depth of ~1000 m where the minimum *in situ* stress is of the order $\sigma_h = 25$ MPa. Thus, the fluid pressure that

propagates the fracture could be only slightly higher than 25 MPa. The temperature of the formation is assumed to be 50 °C. The injected fracturing fluids are assumed to be in thermal equilibrium with the reservoir, avoiding further complexities in accommodating thermal stresses (Wang et al., 2016; Yao et al., 2016; Zhang et al., 2018), anticipated to be negligible. The properties of slickwater, CO_2, N_2, Ethane, and LPG at a pressure of 25 MPa and temperature of 50 °C are listed in Table 2. It can be seen that the density of CO_2 is of a similar magnitude with density of slickwater, while the other gases are much lighter than slickwater with N_2 having the lowest density. The viscosities of all the gases are smaller than the viscosity of slickwater, and again, N_2 exhibits the lowest viscosity. CO_2, N_2 and ethane will all be in a supercritical state during fracturing since both pressure and temperature exceed their critical values, while slickwater and LPG will be in their liquid state.

Permeability, k_{rsv}, and porosity, ϕ_{rsv}, of the formation are assumed to be 10^{-19} m^2 and 0.1, respectively. And initial pore pressure of the reservoir is set as $p_{rsv} = 10$ MPa. The Carter leak-off coefficient (Howard and Fast, 1957) can be written as

$$C_l = \sqrt{\frac{k_{rsv}\phi_{rsv}\Delta p}{2\mu_f}},$$
(15)

where $\Delta p = p_f - p_{rsv}$ is the difference between the fluid pressure in the fracture and the pore pressure in the reservoir. Δp is approximately equal to 15 MPa in this study. According to Eq. (15), the Carter leak-off coefficients of the fluids are calculated and listed in Table 3. Note that, although the Carter leak-off model is widely-used in numerical models, due to its efficiency, the actual leak-off process could be more complex, and thus, measurement of actual leak-off rates would be an important adjunct to this work (Warpinski, 1988; Barree and Mukherjee, 1996).

During the first 1000 s, pure fluid without proppant is injected to initiate and propagate the fracture as a pre-pad fluid. Proppant is then introduced to form a mix of fracturing fluid and proppant particles until 2000s, at which time pumping stops. The injection rate Q_0 is kept as 0.12 m^3/s, and the normalized proppant concentration of the slurry $\overline{\varphi}$ is taken as 0.2. Other parameters used in the calculations are $E = 23.44$ GPa for the Young's modulus, $\nu = 0.25$ for the Poisson's ratio, $H = 50$ m for the fracture height, $\rho_p = 2500$ kg/m^3 for the proppant density, $a = 0.2$ mm for the particle radius, and $\varphi_{max} = 0.585$ for the maximum allowable proppant concentration.

Fig. 3 shows the resulting fracture geometry and corresponding proppant distribution for slickwater fracturing at snapshots in time at $t = 1000$ s, $t = 1250$ s, $t = 1500$ s, $t = 1750$ s and $t = 2000$ s. Note that only one wing of the resulting bi-wing fracture is shown in the figure. After 1000 s of injection of the pre-pad fluid, the fracture propagates to a half-length of ~415 m with a maximum fracture width of ~2.7 mm located at the wellbore. After that, proppant is introduced and transported from wellbore to fracture tip. However, due to the low viscosity of the fracturing fluid, proppant settles rapidly and forms a proppant bank at the fracture base soon after the introduction of the proppant ($t = 1250$ s). Following this, although the fracture continues to propagate, the penetration length of the proppant almost remains unchanged, although the height of the proppant bank continues to grow. At the end of the pumping ($t = 2000$ s), the fracture is ~695 m in length and has a maximum aperture of ~3.4 mm. The proppant

Table 2
Properties of fluids used in this study at a pressure of 25 MPa and temperature of 50 °C. (Note that the slickwater viscosity listed in the table corresponds to a viscosity of 0.001 Pa·s under standard conditions).

Fluids	Density, ρ_f (kg/m^3)	Viscosity, μ_f (Pa·s)	Phase
Slickwater	998.61	5.52E-04	Liquid
CO_2	834.19	7.74E-05	Supercritical
N_2	235.25	2.49E-05	Supercritical
Ethane	403.86	6.10E-05	Supercritical
LPG	514.52	1.13E-04	Liquid

Table 3
Leak-off coefficient of fluids used in this study.

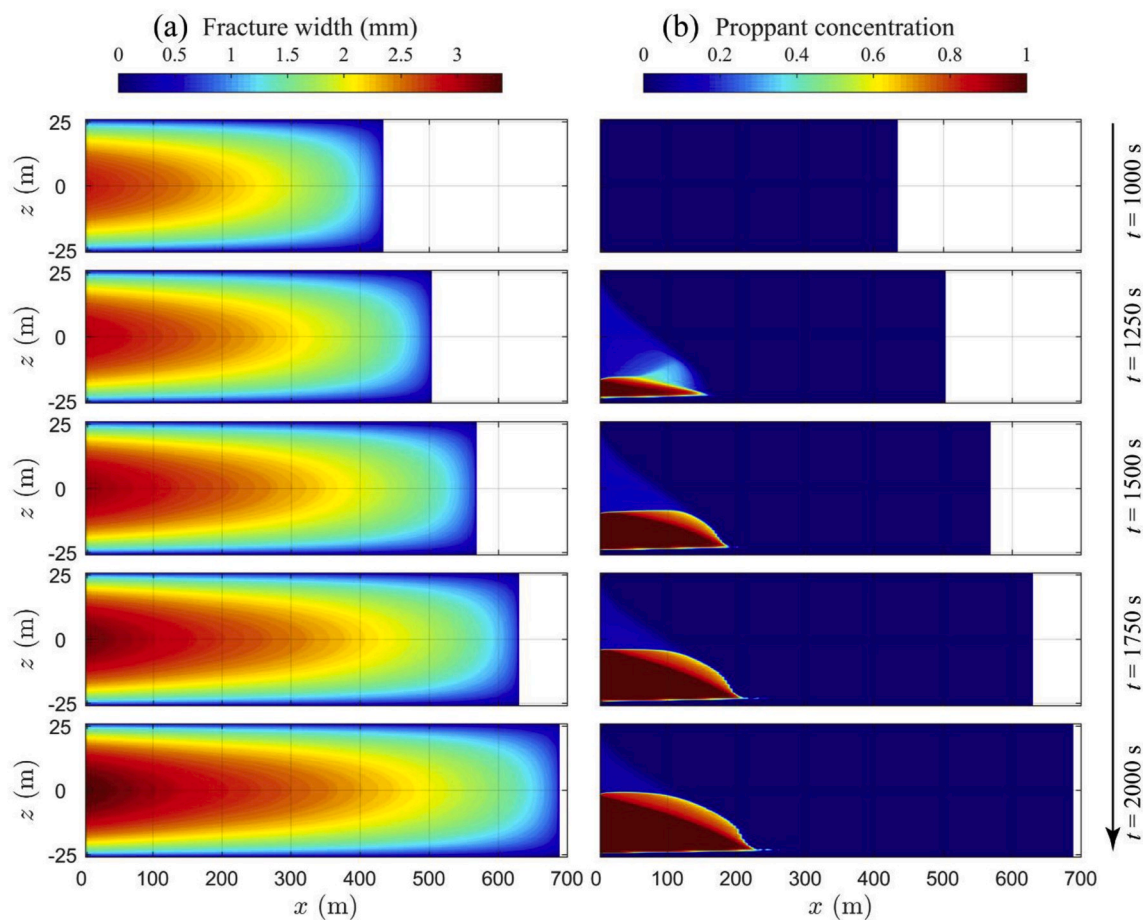| Fluids	Leak-off coefficient, C_l (m/$\sqrt{s}$)
Slickwater	1.17E-05
CO_2	3.11E-05
N_2	5.49E-05
Ethane	3.51E-05
LPG	2.57E-05

Fig. 3. Simulation results for slickwater fracturing at different snapshots in time $t = 1000$ s, $t = 1250$ s, $t = 1500$ s, $t = 1750$ s and $t = 2000$ s: (a) fracture geometry and (b) proppant distribution.

penetrates into the fracture to a depth of ~220 m and accumulates at the fracture base to a height of approximately half of the fracture height. Note that the simulated fracture half-lengths of ~200 m after several hours of pumping may overestimate penetration due to (i) the assumed low leak-off rate representing an ultra-tight formation (permeability of 10^{-19} m^2) and (ii) the assumed absence of secondary fractures – each of which might limit the propagation of the main hydraulic fracture.

Simulations of fracturing with various gases are then performed, where all the input parameters are kept the same as those for the case of slickwater fracturing - excepting the fluid properties (Table 2) and the related leak-off coefficient (Table 3). The simulation results are shown in Fig. 4. It can be seen that, due to the fast leak-off rate, the fractures resulting from gases are shorter and narrower than that driven by slickwater (Fig. 4a). At the conclusion of pumping, the fractures resulting from LPG, CO_2 and ethane are ~400–500 m in half-length and ~1.3–1.7 mm in width (average width at the inlet). And the fracture induced by N_2 has a half-length of only ~290 m and an average width (at the inlet) of only ~0.9 mm, which are even less, respectively, than fifty percent of the length and the width of the slickwater-driven fracture. For proppant transport, both the high viscosity and high density of the fracturing fluid favor a slow settling velocity and hence deep proppant penetration along the fracture. CO_2 has a higher density but a lower viscosity than LPG, and consequently results in a similar proppant penetration length of ~110 m, which is approximately half that resulting from slickwater fracturing (see Fig. 4b). Compared to LPG and CO_2, ethane carries proppant to a shorter length of ~73 m due to its lower viscosity and density. However, for the case of N_2, the proppant concentration within the entire fracture is null because the fracture is too narrow to allow proppant to enter into (screen-out occurs at the inlet).

Admittedly, proppant is carried to relatively shorter distances by gases than by slickwater when the same injection rate is used, but the capability for proppant transport of gases is still potentially acceptable. This is because gas fracturing is commonly operated at higher injection rates than that for slickwater fracturing (Gandossi, 2013; Moridis, 2018). The high-rate injection of gases requires less pumping power and is therefore more achievable than for slickwater, due to the reduced frictional losses resulting from the lower viscosity of gases. A candidate case for CO_2 fracturing with a doubled injection rate ($Q_0 = 0.24$ m^3/s) increases the length of proppant penetration from ~105 m to ~180 m - comparable with that of slickwater at the original injection rate.

3.2. Fracturing with gelled gases

Gases are sometimes gelled to achieve a high and consistent viscosity, to improve the proppant-carrying capacity and to control fluid leak-off. We explore the case of fracturing with gelled CO_2 where the viscosity of CO_2 is increased *via* the dissolution of dilute concentrations (less than 1 wt%) of "thickeners". Ideally, viscosity can be increased by a factor of ~2–100 where chemical additives are non-damaging to the formation, because they would either flow back with the gaseous CO_2 or be of such minimal mass that porosity and permeability of the formation and proppant pack would not be affected (Enick, 1998).

In this simulation, the dynamic viscosity of the gelled CO_2 is 0.01 Pa·s, which is ~18 times that of the slickwater and ~129 times that of pure CO_2. The other input parameters are unchanged from those in Section 3.1. The simulation results are shown and compared with slickwater and pure CO_2 in Fig. 5. The fracture created by the gelled CO_2 is wider but shorter (due to the enhanced viscosity) and has a larger
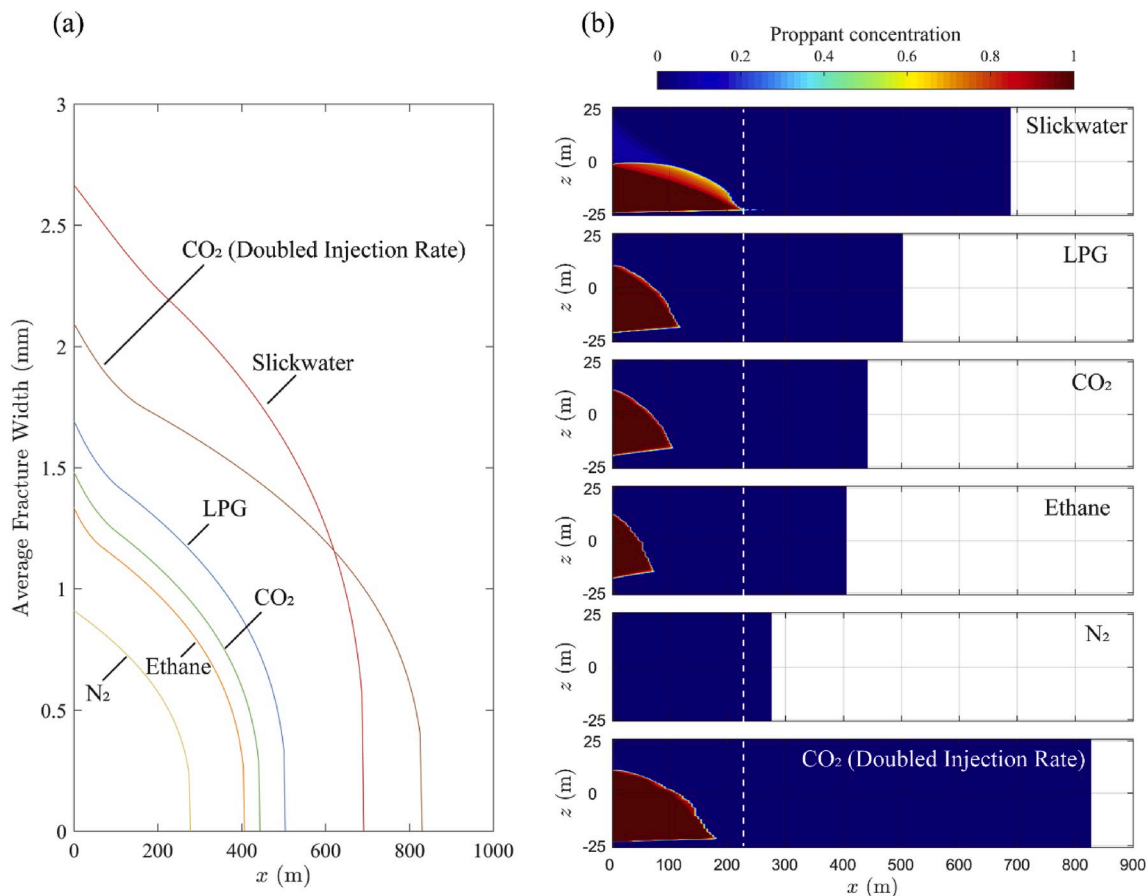
Fig. 4. Simulation results for fracturing with various gases (LPG, CO_2, ethane, and N_2) at the conclusion of pumping ($t = 2000$ s): (a) fracture geometry and (b) proppant distribution. Results of slickwater fracturing are also shown for comparison. The white dashed line represents the length of proppant penetration down-range along the fracture driven by slickwater.
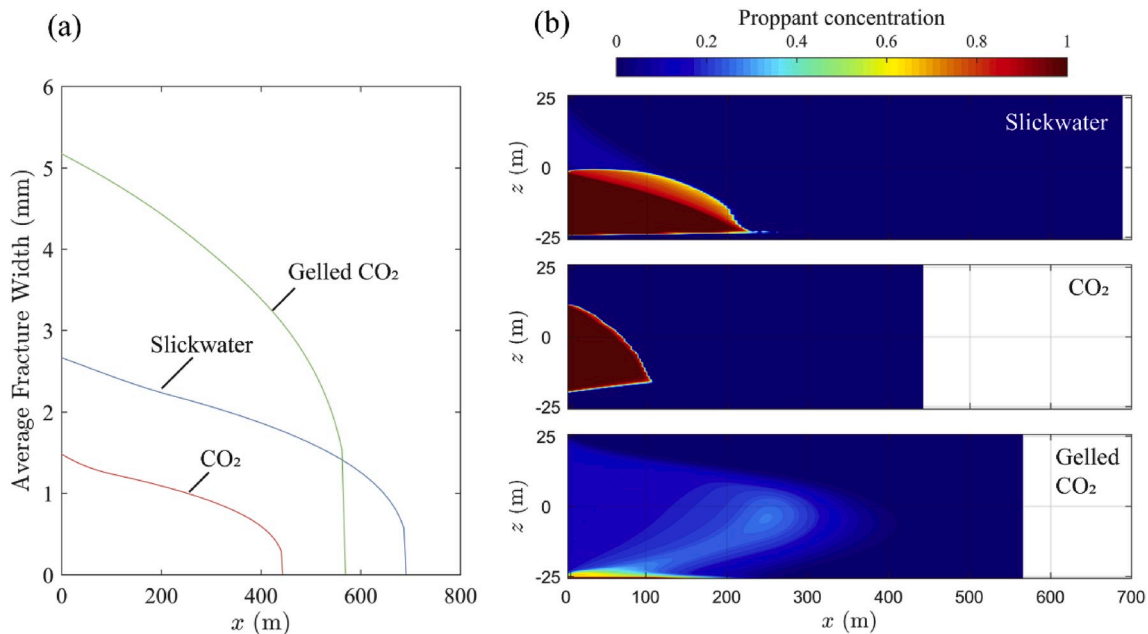

Fig. 5. Simulation results for fracturing with gelled CO_2 at the conclusion of pumping ($t = 2000$ s): (a) fracture geometry and (b) proppant distribution. Results for fracturing with slickwater and pure CO_2 are also shown for comparison.

volume (due to the reduced leak-off rate) than that created by slickwater (Fig. 5a). The proppant-carrying capacity is improved significantly after being gelled. It can be seen that the mixture of the gelled CO_2 and proppant exhibits a "triangular-shaped" proppant distribution within the fracture with a scaled volumetric concentration of ~0.1–0.3. The proppant penetration length is ~400 m which is much deeper than with slickwater and with un-gelled CO_2. Although a small proppant bank is formed at the fracture base, a considerable area of the propped fracture is achieved at the end of the treatment.

3.3. Foam fracturing

Foams are also a good candidate for fracturing unconventional formations because of their capacity to suspend proppant but with intrinsically low water contents. As stated previously, foams normally contain both liquid and gas phases with the two phases combined by applying a suitable foaming surfactant. The liquid phase could be water, acid, or alcohol, while the gas phase is usually N_2 or CO_2. The density and rheological properties of a foam depend on the foam quality, which is defined as the percentage of the internal phase (gas) as

$$Q = \frac{V_g}{V_l + V_g}, \tag{16}$$

where V_g and V_l are the volumes of gas and liquid, respectively.

In this study, a polymer-free N_2 foam with 0.5 wt% anionic surfactant is considered whose rheological properties are previously defined (Gu and Mohanty, 2015). The apparent foam viscosity can by written as

$$\mu_{ap} = K\gamma^{n-1}, \tag{17}$$

where K is the consistency index, γ is the shear rate, and n is a power law index. Here, the consistency index and the power law index are dependent on foam quality and fluid pressure (in psi) as

$$K = \begin{cases} 10^{(5.89Q^2 + 0.43Q) - 4} & 0 \le Q < 0.6 \\ 10^{(5.89Q^2 + 0.43Q) - 4} + 8.6 \times 10^{-11} e^{21Q}(p_f - 1000) & 0.6 \le Q < 0.85 \end{cases} \tag{18}$$

and

$$n = \begin{cases} (1.54 - 1.64Q^2) & 0 \le Q < 0.6 \\ (1.54 - 1.64Q^2) - (0.89Q - 0.21)[\log(p_f/1000)] & 0.6 \le Q < 0.85 \end{cases}. \tag{19}$$

Foam density can be calculated by

$$\rho_{foam} = \rho_l - Q(\rho_l - \rho_g), \tag{20}$$

where ρ_l and ρ_g are the densities of the liquid (water) and gas (N_2), respectively. A typical fracturing shear rate $\gamma = 511$ s^{-1} and an averaged fluid pressure $p_f = 25$ MPa are used in the calculations.

Typically, foam quality is in the range of ~50%–95%, and the fracturing fluid is considered as energized if the percentage of the gas volume is below 50% (Moridis, 2018). However, in addition to foam qualities of 50% and 80%, a foam quality of 20% is also considered here to observe the overall trend. The simulation results are shown in Fig. 6 and are compared with the case of fracturing with slickwater where density and rheological properties are close to a foam of quality of 0%. It can be seen that the 0%-quality foam (slickwater) creates the longest but narrowest fracture due to its lowest viscosity. As the foam quality increases, the viscosity of the foam increases resulting in a decreasing fracture length and an increasing fracture width (Fig. 6a). As can be seen from Fig. 6b, the proppant is distributed more uniformly in the vertical direction by a foam with a higher quality - due to the reduced settling velocity of the proppant. A near-uniform proppant distribution is achieved by the 80%-quality foam when pumping stops, although the proppant penetration along the fracture is not as deep as those resulting from 20%- to 50%-quality foams.
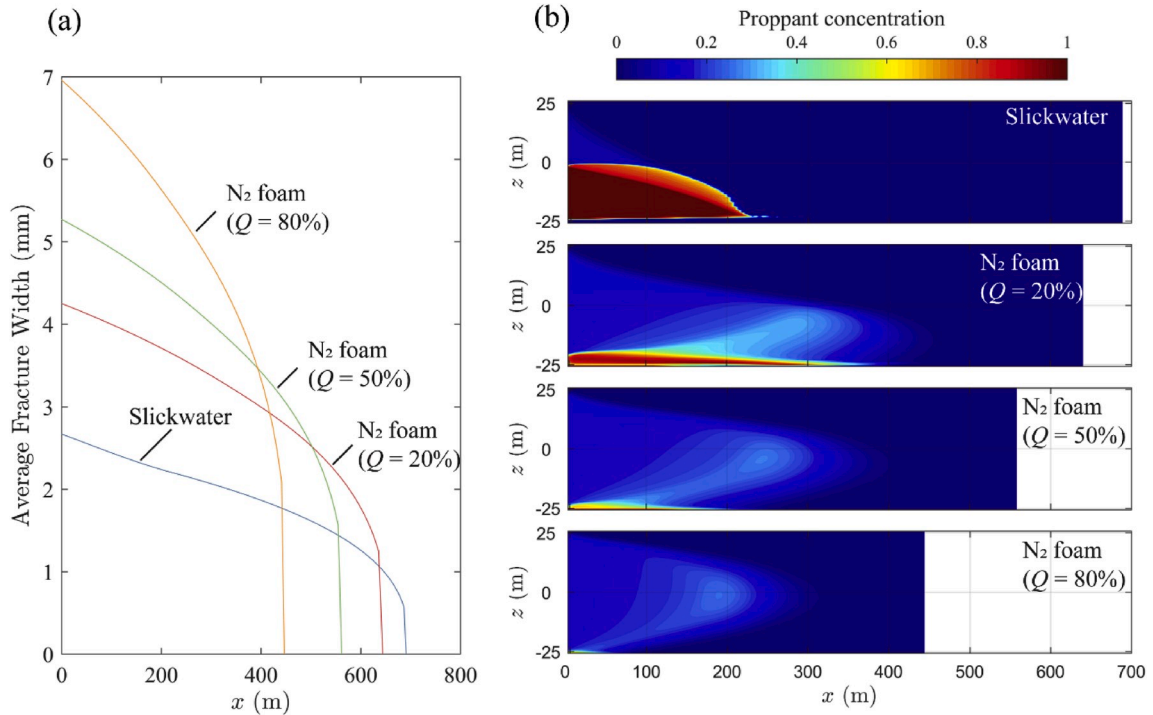

Fig. 6. Simulation results for fracturing with N_2 foam at the conclusion of pumping ($t = 2000$ s): (a) fracture geometry and (b) proppant distribution. Results for slickwater fracturing are also shown for comparison.

3.4. Ultra-light-weight proppant

Ultra-light-weight proppants (ULWPs) are proppants with a low density, relative to normal sands (S.G. ~2.7) and relative to the fracturing fluid. These proppants are fabricated by coating strong materials with light materials, creating significant porosity inside hard materials, or directly using polymers as raw material for the proppant (Brannon and Starks, 2009; Gaurav et al., 2010). They are normally 25%–60% lighter than commonly-used sands (Gu et al., 2015). A ULWP with a density of 1050 kg/m^3 is combined with CO_2 fracturing in this work, and again, the other input parameters remain unchanged from those in Section 3.1. The distribution of the ULWP placed by CO_2 are shown and compared with the commonly-used sand in Fig. 7. The resulting fracture geometries are not shown here as the two cases of CO_2 fracturing return near-identical fracture geometry (see the case of CO2 fracturing in Fig. 5a) regardless of the difference in proppant density. This indicates that the effect of proppant density on the fracture geometry is negligible. At the end of the pumping, the ULWP carried by CO_2 shows a deeper penetration along the fracture than the commonly-used sand carried either by slickwater or by CO_2 – this is principally due to the slower settling velocity resulting from the lower density contrast between proppant and fracturing fluid. Thus, the ULWPs show some promise in use with fracturing by gases relative to the more commonly-used sands.

3.5. Fracture closure and gas production

At the conclusion of pumping, fluid pressure decreases, enabling hydraulic fractures to close and compact the encased proppant packs. We define fracture closure for all 11 cases discussed in Sections 3.1-3.4 by applying the fracture closure model (Section 2.3) with the input

Table 4
Input parameters for fracture closure simulations.

Parameters	Values
Minimum *in-situ* stress, σ_h	25 MPa
Compressibility of proppant pack, c_p	7.25×10^{-9} Pa^{-1}
Asperity width, w_a	0.1 mm
Asperity compliance, b_1	1.43×10^{-11} Pa^{-1}

parameters listed in Table 4. Note that c_p represents the skeletal compressibility of the proppant pack (assembly of proppant particles), which is much larger than that of an individual proppant particle. As an illustration, Fig. 8 shows residual aperture, conductivity, and residual porosity of the slickwater-driven fracture as the hydraulic pressure decreases to 5 MPa. It can be seen that the proppant props open a portion of the fracture providing a relatively high fracture conductivity for gas to be recovered. Interestingly, this is further promoted by the high-conductivity channels formed around the proppant bank due to the flexural displacement of the unsupported spans of the fracture (Wang et al., 2018a). Fracture residual porosity is ~0.3 for the propped portion and equal to 1 for the unpropped portion. The other cases present similar results for fracture closure but are not shown here for brevity.

The residual apertures, w_r, conductivities, C_f, and porosity, n_r, of the closed fractures recovered from the fracture closure simulations are then input into a reservoir simulation model to predict the productivities of fractured wells. Fig. 9 shows the reservoir-fracture domain for this reservoir simulation model. Taking advantage of the symmetry, only one wing of a fracture and half the matrix between the two adjacent fractures are simulated. The governing equations for gas flow within the reservoir
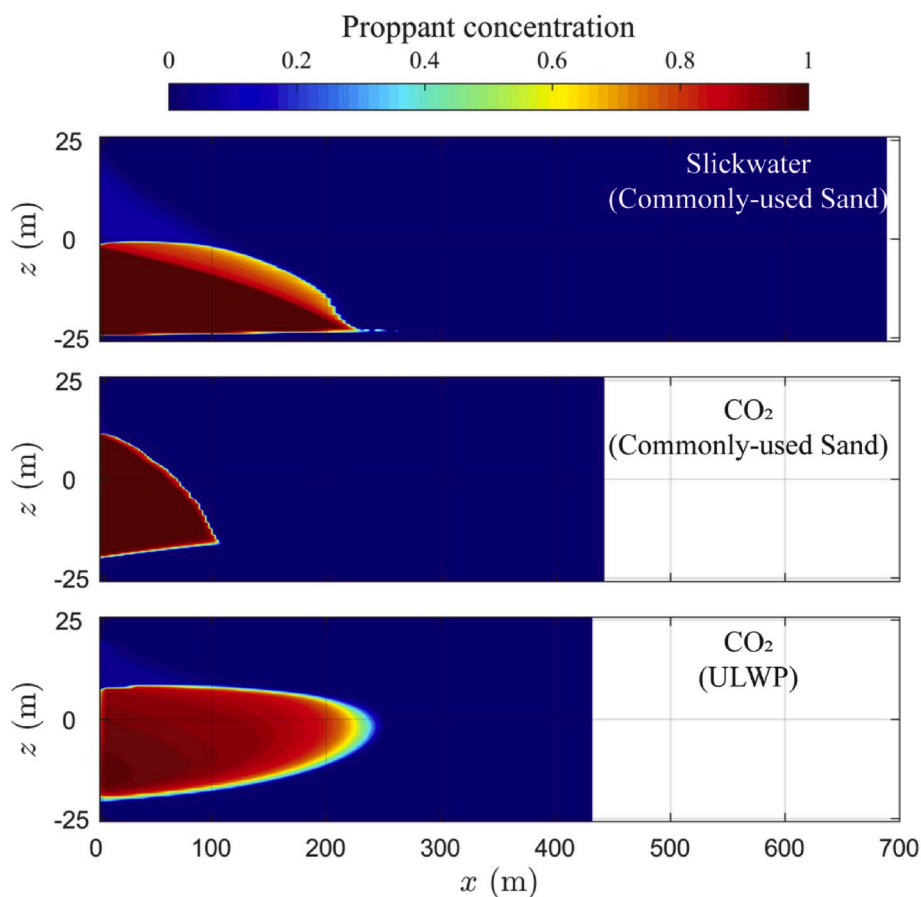
Fig. 7. Distribution of ULWP at the conclusion of pumping ($t = 2000$ s) for CO_2 fracturing. Results for slickwater fracturing and CO_2 fracturing with commonly-used sand are also shown for comparison.
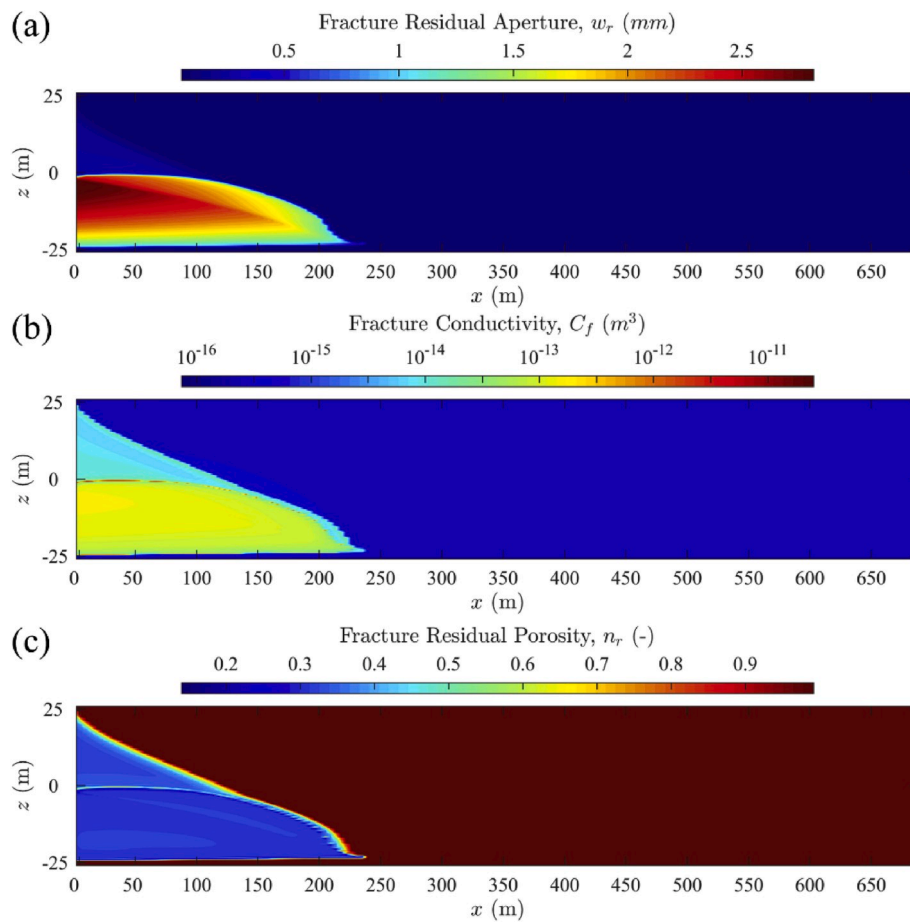
Fig. 8. (a) Residual aperture, (b) conductivity, and (c) residual porosity of the slickwater-driven fracture as the hydraulic pressure decreases to 5 MPa.
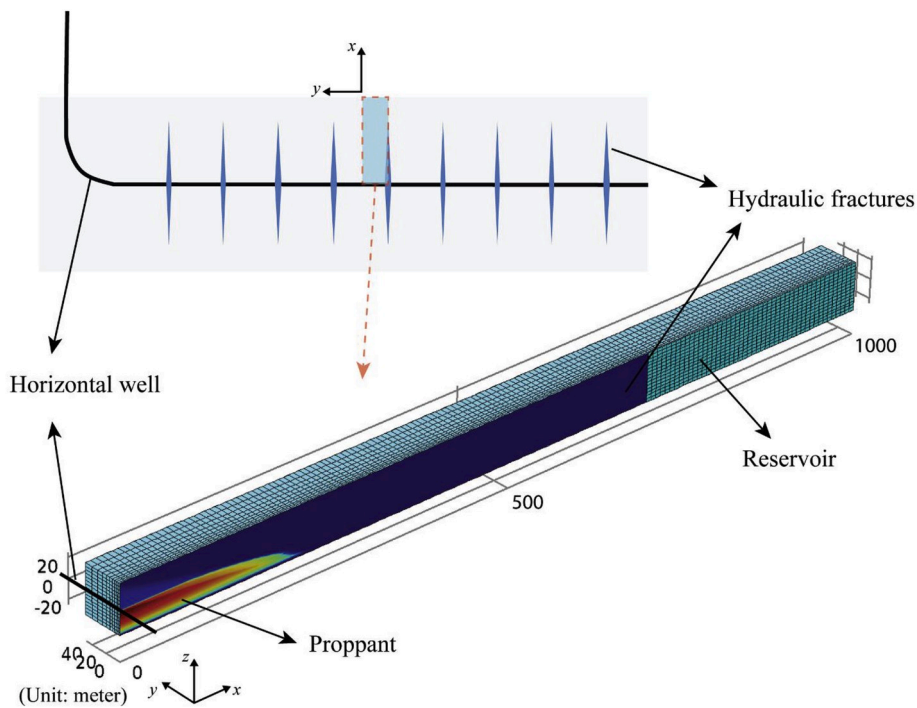

Fig. 9. Schematic of the reservoir-fracture domain for the reservoir simulation model.

and the fracture can be expressed, respectively, as (Wang et al., 2018a)

$$\varphi_{rsv}\rho_g c_g \frac{\partial p_{rsv}}{\partial t} + \nabla \cdot \left(-\frac{k_{rsv}}{\mu_g}\rho_g \nabla p_{rsv} \right) = 0, \tag{21}$$

and

$$w_r \phi_r \rho_g c_g \frac{\partial p_f}{\partial t} + \nabla \cdot \left(-\frac{C_f}{\mu_g}\rho_g \nabla p_f \right) = 2\frac{k_{rsv}}{\mu_g}\rho_g \nabla p_{rsv}\bigg|_{y=0}, \tag{22}$$

where p_{rsv} and p_f are two unknown pressures in the reservoir and fracture, respectively; ρ_g and c_g are density and compressibility of methane, respectively, and are functions of fluid pressure which can be obtained from the NIST database (Lemmon, 1998); μ_g is the dynamic viscosity of methane. Eq. (21) is defined in the entire 3D domain (Fig. 9) where all the boundaries are set as no flow excepting $p_{rsv}(x,z)|_{y=0} = p_f(x,z)$. And Eq. (22) is defined only in the hydraulic fracture which is pierced by a production well at the origin with the other boundaries set as no flow. The reservoir simulation model is solved by using COMSOL Multiphysics with the input parameters listed in Table 5.

Fig. 10 shows cumulative gas production from a single fracture with time for a 3-year period. As expected, fracturing with pure gases returns lower production rates than with slickwater when the fluids are pumped at the same rate, since gases generate shorter fractures and shorter proppant penetrations. However, this inefficiency of gas fracturing could be offset by an elevated injection rate, as demonstrated by the similar cumulative gas production volumes resulting from slickwater fracturing with the base-case original injection rate and CO_2 fracturing with a doubled injection rate. The production rate is enhanced significantly by fracturing with gelled gases and foams, primarily due to the relatively uniform proppant distribution and effective control of leak-off – promoting the effective lengthening of the fluid-driven fracture. Among the three cases of foam fracturing with different qualities, although the 80%-quality foam delivers the most uniform proppant distribution, the 20%-quality foam results in the highest production rate. This is possibly because, for the ultra-low-permeability reservoir, a long fracture with relatively low conductivity favors higher flow rates than a short one with high conductivity. The improvement of gas production by using ULWPs instead of normal sands with gases is also be observed, however, it is limited by the short fractures resulting from the fast leak-off of the pure gases.

4. Conclusion

Fracture propagation and proppant transport driven by commonly-used pure gases (CO_2, LPG, ethane, and N_2) are investigated relative to the behavior for routine slickwater fracturing. The generally degraded performance of gas fracturing relative to slickwater fracturing is explored in terms of mechanistic controls. Based on these mechanisms, several methods to improve the proppant-carrying capacity of the pure gases are examined, including the employments of gelled gases, foam-systems, and ultra-light-weight proppants.

During fluid-driven fracturing, the gases are principally in their liquid or supercritical phases. Relative to slickwater, they exhibit lower
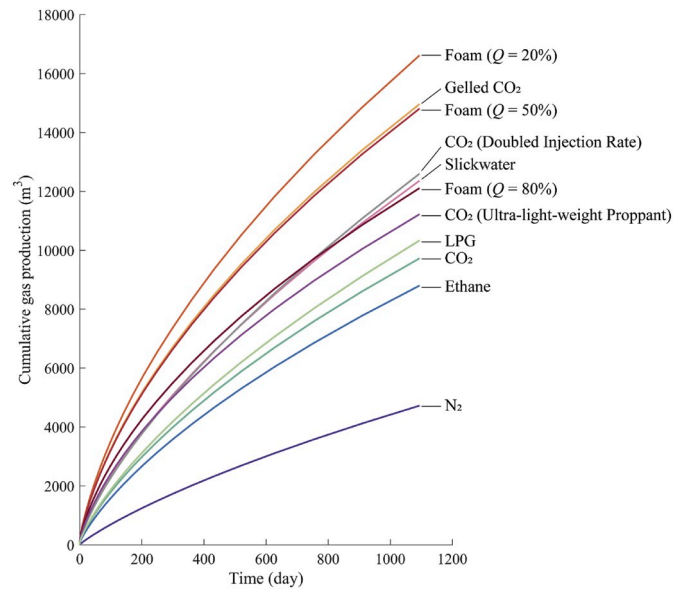
Table 5
Input parameters for reservoir simulations.

Parameters	Values
Hydraulic fracture spacing, s_f	100 m
Wellbore diameter, d_w	0.25 m
Reservoir porosity, ϕ_{rsv}	0.1
Reservoir permeability, k_{rsv}	1×10^{-19} m^2
Initial pore pressure, p_{rsv0}	10 MPa
Dynamic viscosity of methane, μ_g	1.19×10^{-5} Pa·s
Bottomhole pressure (BHP), p_{BHP}	3 MPa

Fig. 10. Cumulative gas production versus time for a 3-year period.

viscosities and densities, which in turn results in faster leak-off rates and more severe proppant settling. Consequently, at the same injection rate and at the conclusion of pumping, the gas-driven fractures are shorter and narrower and encase shorter proppant banks than the slickwater-driven fractures. Among the gases examined in this study, LPG and CO_2 return the deepest proppant penetration along the fracture, followed by ethane, with N_2 unable to carry proppant into the fracture due to the resulting narrow fracture. However, the proppant-carrying capacity of gases may still be acceptable, because gas fracturing can be operated at higher injection rates than slickwater fracturing due to the lower frictional losses during fluid flow both down the well and along the evolving fracture. Simulation results show that CO_2 could have a proppant-carrying capacity competitive with slickwater by merely doubling the injection rate.

Viscosity of gases can be enhanced by adding trace amounts of "thickeners" to form a gelled system or by mixing a gas with a liquid to obtain a foam-based fluid. The enhanced viscosity not only reduces the leak-off rate, which increases both the length and width of the fracture, but also improves the proppant-carrying capacity of the gases by slowing proppant settling. The proppant carried by gelled CO_2 (with a viscosity ~128 times higher than un-gelled CO_2) is distributed relatively uniformly within the fracture and with a much deeper penetration than for either pure CO_2 or slickwater. Foams with increasing quality distribute the proppant progressively more uniformly in the vertical direction with a near-uniform proppant distribution resulting from a relatively high-quality foam. ULWPs have densities much lower than the commonly-used sand. A ULWP with a density of 1050 kg/m^3 offsets the low viscosity of the carrying fluid (CO_2), resulting in a considerably large propped area for the fracture at the conclusion of the pumping.

Reservoir simulations show that fracturing with pure gases returns lower production rates than with slickwater when the fluids are injected at the same rate. This inefficiency of gas fracturing can be compensated by elevating the injection rate during operation, which may be capable of increasing the resulting production rate to a magnitude comparable to that of slickwater fracturing or even higher. Well performance is improved significantly by fracturing with gelled gases or foams instead of pure gases or by pumping ULWPs instead of normal sands. Among them, the low-quality foam returns the highest production rate, while the ULWP returns the lowest. This is possibly because a long fracture with relatively low conductivity favors increased flow over the case of a short fracture with high conductivity for the ultra-low-permeability reservoir.

Declaration of competing interest

The authors declare that they have no known competing financial interests or personal relationships that could have appeared to influence the work reported in this paper.

CRediT authorship contribution statement

Jiehao Wang: Conceptualization, Methodology, Software, Validation, Formal analysis, Investigation, Writing - original draft. **Derek Elsworth:** Conceptualization, Methodology, Supervision, Writing - review & editing.

Appendix A. Supplementary data

Supplementary data to this article can be found online at https://doi.org/10.1016/j.jngse.2020.103269.

References

Adachi, J., Siebrits, E., Peirce, A., Desroches, J., 2007. Computer simulation of hydraulic fractures. Int. J. Rock Mech. Min. Sci. 44, 739–757. https://doi.org/10.1016/j.ijrmms.2006.11.006.

Bandis, S.C., Lumsden, A.C., Barton, N.R., 1983. Fundamentals of rock joint deformation. Int. J. Rock Mech. Min. Sci. 20, 249–268. https://doi.org/10.1016/0148-9062(83)90595-8.

Barree, R., Mukherjee, H., 1996. Determination of pressure dependent leakoff and its effect on fracture geometry. SPE Annu. Tech. Conf. 10 https://doi.org/10.2118/36424-MS.

Barton, N., Bandis, S., Bakhtar, K., 1985. Strength, deformation and conductivity coupling of rock joints. Int. J. Rock Mech. Min. Sci. 22, 121–140. https://doi.org/10.1016/0148-9062(85)93227-9.

Bennour, Z., Watanabe, S., Chen, Y., Ishida, T., Akai, T., 2017. Evaluation of stimulated reservoir volume in laboratory hydraulic fracturing with oil, water and liquid carbon dioxide under microscopy using the fluorescence method. Geomech. Geophys. Geo-Energy Geo-Resources i 4 (1), 39–50. https://doi.org/10.1007/s40948-017-0073-3.

Brannon, H.D., Starks, T.R., 2009. Maximizing return on fracturing investment by using ultra-lightweight proppants to optimize effective fracture area: can less really deliver more? Soc. Pet. Eng. - SPE Hydraul. Fract. Technol. Conf. 2009 441–453. https://doi.org/10.2118/119385-ms.

Carrier, B., Granet, S., 2012. Numerical modeling of hydraulic fracture problem in permeable medium using cohesive zone model. Eng. Fract. Mech. 79, 312–328. https://doi.org/10.1016/j.engfracmech.2011.11.012.

Chen, Z., Bunger, A.P., Zhang, X., Jeffrey, R.G., 2009. Cohesive zone finite element-based modeling of hydraulic fractures. Acta Mech. Solida Sin. 22, 443–452. https://doi.org/10.1016/S0894-9166(09)60295-0.

Damjanac, B., Cundall, P., 2016. Application of distinct element methods to simulation of hydraulic fracturing in naturally fractured reservoirs. Comput. Geotech. 71, 283–294. https://doi.org/10.1016/j.compgeo.2015.06.007.

Detournay, E., 2016. Mechanics of hydraulic fractures. Annu. Rev. Fluid Mech. 48, 311–339. https://doi.org/10.1146/annurev-fluid-010814-014736.

Dontsov, E.V., Peirce, a.P., 2014. Slurry flow, gravitational settling and a proppant transport model for hydraulic fractures. J. Fluid Mech. 760, 567–590. https://doi.org/10.1017/jfm.2014.606.

Dontsov, E.V., Peirce, A.P., 2015a7. An enhanced pseudo-3D model for hydraulic fracturing accounting for viscous height growth, non-local elasticity, and lateral toughness. Eng. Fract. Mech. 142, 116–139. https://doi.org/10.1016/j.engfracmech.2015.05.043.

Dontsov, E.V., Peirce, A.P., 2015b. A Lagrangian approach to modelling proppant transport with tip screen-out in KGD hydraulic fractures. Rock Mech. Rock Eng. 48, 2541–2550. https://doi.org/10.1007/s00603-015-0835-6.

Ellsworth, W., 2013. Injection-induced earthquakes. Science (80-.) 341, 142. https://doi.org/10.1785/gssrl.83.2.250.

Elsworth, D., Spiers, C.J., Niemeijer, A.R., 2016. Understanding induced seismicity. Science (80- 354, 1380–1381. https://doi.org/10.1126/science.aal2584.

Enick, R.M., 1998. A Literature Review of Attempts to Increase the Viscosity of Dense Carbon Dioxide. US DOE NETL Rep. DE-AP26-97FT25356.

Gallegos, T.J., Varela, B.A., Haines, S.S., Engle, M.A., 2015. Hydraulic fracturing water use variability in the United States and potential environmental implications. Water Resour. Res. 51, 5839–5845. https://doi.org/10.1002/2015WR017278.

Gan, Q., Elsworth, D., Alpern, J.S., Marone, C., Connolly, P., 2015. Breakdown pressures due to infiltration and exclusion in finite length boreholes. J. Petrol. Sci. Eng. 127, 329–337. https://doi.org/10.1016/j.petrol.2015.01.011.

Gandossi, L., 2013. An Overview of Hydraulic Fracturing and Other Formation Stimulation Technologies for Shale Gas Production, European Commission Joint Research Center Technical Reports. https://doi.org/10.2790/99937.

Gaurav, A., Dao, E.K., Mohanty, K.K., 2010. Ultra-lightweight proppants in shale gas fracturing. Soc. Pet. Eng. - SPE Tight Gas Complet. Conf. 2010 265–277. https://doi.org/10.2118/138319-ms.

Ghaderi, A., Taheri-Shakib, J., Sharif Nik, M.A., 2018. The distinct element method (DEM) and the extended finite element method (XFEM) application for analysis of interaction between hydraulic and natural fractures. J. Petrol. Sci. Eng. 171, 422–430. https://doi.org/10.1016/j.petrol.2018.06.083.

Gordeliy, E., Peirce, A., 2013. Coupling schemes for modeling hydraulic fracture propagation using the XFEM. Comput. Methods Appl. Mech. Eng. 253, 305–322. https://doi.org/10.1016/j.cma.2012.08.017.

Greetesma, J., de Klerk, F., 1969. A rapid method of predicting width and extent of hydraulic induced fractures. J. Petrol. Technol. 21, 1571–1581.

Gu, M., Dao, E., Mohanty, K.K., 2015. Investigation of ultra-light weight proppant application in shale fracturing. Fuel 150, 191–201. https://doi.org/10.1016/j.fuel.2015.02.019.

Gu, M., Mohanty, K.K., 2015. Rheology of polymer-free foam fracturing fluids. J. Petrol. Sci. Eng. 134, 87–96. https://doi.org/10.1016/j.petrol.2015.07.018.

Howard, G., Fast, C.R., 1957. Optimum fluid characteristics for fracture extension. Proc. Am. Pet. Inst. 261–270. https://www.onepetro.org/conference-paper/API-57-261.

Ishida, T., Chen, Y., Bennour, Z., Yamashita, H., Inui, S., Nagaya, Y., Naoi, M., Chen, Q., Nakayama, Y., Nagano, Y., 2016. Features of CO$_2$ fracturing deduced from acoustic emission and microscopy in laboratory experiments. J. Geophys. Res. Solid Earth 121 (11), 8080–8098. https://doi.org/10.1002/2016JB013365.

Khristianovic, S.A., Zheltov, Y.P., 1955. Formation of vertical fractures by means of highly viscous liquid. In: Proceeding of the 4th World Petroleum Congress, pp. 579–586.

King, S.R., 1983. Liquid CO2 for the stimulation of low-permeability reservoirs. Proc. SPE/DOE Low Permeability Gas Reserv. Symp. https://doi.org/10.2523/11616-MS. SPE 11616.

Kovalyshen, Y., Detournay, E., 2010. A reexamination of the classical PKN model of hydraulic fracture. Transport Porous Media 81, 317–339. https://doi.org/10.1007/s11242-009-9403-4.

Lecampion, B., Bunger, A., Zhang, X., 2018. Numerical methods for hydraulic fracture propagation: a review of recent trends. J. Nat. Gas Sci. Eng. 49, 66–83. https://doi.org/10.1016/j.jngse.2017.10.012.

Lemmon, E.W., 1998. Thermophysical properties of fluid systems. NIST Chem. WebBook. Number 69 20899.

Li, X., Feng, Z., Han, G., Elsworth, D., Marone, C., Saffer, D., Cheon, D.-S., 2016. Breakdown pressure and fracture surface morphology of hydraulic fracturing in shale with H2O, CO2 and N2. Geomech. Geophys. Geo-Energy Geo-Resources 1–8. https://doi.org/10.1007/s40948-016-0022-6.

Lillies, A.T., King, S.R., 1982. Sand fracturing with liquid carbon dioxide. In: SPE Production Technology Symposium. Society of Petroleum Engineers. https://doi.org/10.2523/11341-ms.

Liu, R., Jiang, Y., Huang, N., Sugimoto, S., 2018b. Hydraulic properties of 3D crossed rock fractures by considering anisotropic aperture distributions. Adv. Geo-Energy Res. 2, 113–121. https://doi.org/10.26804/ager.2018.02.01.

Liu, L., Zhu, W., Wei, C., Elsworth, D., Wang, J., 2018a. Microcrack-based geomechanical modeling of rock-gas interaction during supercritical CO2 fracturing. J. Petrol. Sci. Eng. 164, 91–102. https://doi.org/10.1016/j.petrol.2018.01.049.

Middleton, R.S., Carey, J.W., Currier, R.P., Hyman, J.D., Kang, Q., Karra, S., Jiménez-Martínez, J., Porter, M.L., Viswanathan, H.S., 2015. Shale gas and non-aqueous fracturing fluids: opportunities and challenges for supercritical CO2. Appl. Energy 147, 500–509. https://doi.org/10.1016/j.apenergy.2015.03.023.

Moridis, G., 2018. Literature Review and Analysis of Waterless Fracturing Methods. Berkeley, CA (United States).

Nordgren, R.P., 1972. Propagation of a vertical hydraulic fracture. Soc. Petrol. Eng. J. 12, 306–314. https://doi.org/10.2118/3009-PA.

Osiptsov, A.A., 2017. Fluid mechanics of hydraulic fracturing: a review. J. Petrol. Sci. Eng. 156, 513–535. https://doi.org/10.1016/j.petrol.2017.05.019.

Ouyang, S., Carey, G.F., Yew, C.H., 1997. An adaptive finite element scheme for hydraulic fracturing with proppant transport. Int. J. Numer. Methods Fluids 24, 645–670. https://doi.org/10.1002/(sici)1097-0363(19970415)24:7<645::aid-fld458>3.0.co;2-z.

Palisch, T.T., Vincent, M., Handren, P.J., 2010. Slickwater fracturing: food for thought. SPE Prod. Oper. 25, 327–344. https://doi.org/10.2118/115766-PA.

Park, Y., Dreuzy, J. De, Lee, K., 2001. Transport and intersection mixing in random fracture networks with power law length distributions. Water Resour. Res. 37, 2493–2501.

Perkins, T.K., Kern, L.R., 1961. Widths of hydraulic fractures. J. Petrol. Technol. 13, 937–949. https://doi.org/10.2118/89-PA.

Shiozawa, S., McClure, M., 2016. Simulation of proppant transport with gravitational settling and fracture closure in a three-dimensional hydraulic fracturing simulator. J. Petrol. Sci. Eng. 138, 298–314. https://doi.org/10.1016/j.petrol.2016.01.002.

Tada, H., Paris, P.C., Irwin, G.R., 2000. Two-Dimensional stress solutions for various configurations with cracks. In: The Stress Analysis of Cracks Handbook. ASME Press.

Taleghani, A.D., Gonzalez, M., Shojaer, A., 2016. Overview of numerical models for interactions between hydraulic fractures and natural fractures: challenges and limitations. Comput. Geotech. 71, 361–368. https://doi.org/10.1007/s10499-012-9533-5.

Tudor, E.H., Nevison, G.W., Allen, S., Pike, B., 2009. 100% Gelled LPG Fracturing Process: an Alternative to Conventional Water-Based Fracturing Techniques. SPE East. Reg. Meet. m. https://doi.org/10.2118/124495-MS.

Wang, J., Elsworth, D., 2018. Role of proppant distribution on the evolution of hydraulic fracture conductivity. J. Petrol. Sci. Eng. 166, 249–262. https://doi.org/10.1016/j.petrol.2018.03.040.

Wang, J., Elsworth, D., Cao, Y., Liu, S., 2020. Reach and geometry of dynamic gas-driven fractures. Int. J. Rock Mech. Min. Sci. 129, 104287. https://doi.org/10.1016/0148-9062(84)90002-0.

Wang, J., Elsworth, D., Denison, M.K., 2018a. Propagation, proppant transport and the evolution of transport properties of hydraulic fractures. J. Fluid Mech. 855, 503–534. https://doi.org/10.1017/jfm.2018.670.

Wang, J., Elsworth, D., Denison, M.K., 2018b. Hydraulic fracturing with leakoff in a pressure-sensitive dual porosity medium. Int. J. Rock Mech. Min. Sci. 107, 55–68. https://doi.org/10.1016/j.ijrmms.2018.04.042.

Wang, J., Elsworth, D., Wu, Y., Liu, J., Zhu, W., Liu, Y., 2018c. The influence of fracturing fluids on fracturing processes: a comparison between water, oil and SC-CO2. Rock Mech. Rock Eng. 51, 299–313. https://doi.org/10.1007/s00603-017-1326-8.

Wang, L., Yao, B., Cha, M., Alqahtani, N.B., Patterson, T.W., Kneafsey, T.J., Miskimins, J. L., Yin, X., Wu, Y.S., 2016. Waterless fracturing technologies for unconventional reservoirs-opportunities for liquid nitrogen. J. Nat. Gas Sci. Eng. 35, 160–174. https://doi.org/10.1016/j.jngse.2016.08.052.

Wanniarachchi, W.A.M., Ranjith, P.G., Perera, M.S.A., 2017. Shale gas fracturing using foam-based fracturing fluid: a review. Environ. Earth Sci. 76, 91. https://doi.org/10.1007/s12665-017-6399-x.

Wanniarachchi, W.A.M., Ranjith, P.G., Perera, M.S.A., Lashin, A., Al Arifi, N., Li, J.C., 2015. Current opinions on foam-based hydro-fracturing in deep geological reservoirs. Geomech. Geophys. Geo-Energy Geo-Resources 1, 121–134. https://doi.org/10.1007/s40948-015-0015-x.

Warpinski, N.R., 1988. Dual leakoff behavior in hydraulic fracturing of tight, lenticular gas sands. Soc. Pet. Eng. AIME, SPE PI 765–778, 18259.

Xu, C., Kang, Y., You, Z., Chen, M., 2016. Review on formation damage mechanisms and processes in shale gas reservoir: known and to be known. J. Nat. Gas Sci. Eng. 36, 1208–1219. https://doi.org/10.1016/j.jngse.2016.03.096.

Yao, B., Wang, L., Yin, X., Wu, Y.-S., 2016. Numerical modeling of cryogenic fracturing process on laboratory-scale Niobrara shale samples. J. Nat. Gas Sci. Eng. 48, 169–177. https://doi.org/10.1016/j.jngse.2016.10.041.

Zeng, J., Li, H., Zhang, D., 2016. Numerical simulation of proppant transport in hydraulic fracture with the upscaling CFD-DEM method. J. Nat. Gas Sci. Eng. 33, 264–277. https://doi.org/10.1016/j.jngse.2016.05.030.

Zhang, F., Damjanac, B., Maxwell, S., 2019a. Investigating hydraulic fracturing complexity in naturally fractured rock masses using fully coupled multiscale numerical modeling. Rock Mech. Rock Eng. 52, 5137–5160. https://doi.org/10.1007/s00603-019-01851-3.

Zhang, Q., Ma, D., Liu, J., Wang, J., Li, X., Zhou, Z., 2019b. Numerical simulations of fracture propagation in jointed shale reservoirs under CO2 Fracturing. Geofluids 2019, 2624716. https://doi.org/10.1155/2019/2624716.

Zhang, Q., Ma, D., Wu, Y., Meng, F., 2018. Coupled thermal-gas-mechanical (TGM) model of tight sandstone gas wells. J. Geophys. Eng. 15, 1743–1752.

Zhang, F., Dontsov, E., Mack, M., 2017a. Fully coupled simulation of a hydraulic fracture interacting with natural fractures with a hybrid discrete-continuum method. Int. J. Numer. Anal. Methods GeoMech. 41, 1430–1452. https://doi.org/10.1002/nag.2682.

Zhang, G., Gutierrez, M., Li, M., 2017b. Numerical simulation of transport and placement of multi-sized proppants in a hydraulic fracture in vertical wells. Granul. Matter 19, 1–15. https://doi.org/10.1007/s10035-017-0718-5.

Zhang, X., Jeffrey, R.G., Thiercelin, M., 2007. Deflection and propagation of fluid-driven fractures at frictional bedding interfaces: a numerical investigation. J. Struct. Geol. 29, 396–410. https://doi.org/10.1016/j.jsg.2006.09.013.